Dynamical Theory of Angle-Resolved Electron Energy Loss and Gain Spectroscopies of Phonons and Magnons in Transmission Electron Microscopy Including Multiple Scattering Effects

José Ángel Castellanos-Reyes,* Paul M. Zeiger,† and Ján Rusz‡
Department of Physics and Astronomy, Uppsala University, Box 516, 75120 Uppsala, Sweden

(Received 22 February 2024; revised 28 June 2024; accepted 9 December 2024; published 22 January 2025)

We present a method for computing angle-resolved electron energy loss and gain spectroscopies for phonon and magnon excitations in transmission electron microscopy. Fractional scattering intensities are derived from the temperature-dependent time autocorrelation of the auxiliary electron beam wave function. This method captures both single and multiple scattering processes, as well as dynamical diffraction effects, while remaining computationally efficient and easy to parallelize.

DOI: 10.1103/PhysRevLett.134.036402

Recent instrumental advances in scanning transmission electron microscopy (STEM; [1,2]) have enabled the study of low-energy excitations, including phonons. Electron energy loss and gain spectroscopies (EELS and EEGS, respectively) frequently emerge as preferred methods, especially when high spatial resolution is a priority. While reflection electron energy loss spectroscopy is effective at surfaces and in high-resolution contexts [3,4], it is limited by the low penetration depth of low-energy electrons, typically not exceeding 10 eV, which restricts it to surface or ultrathin film studies. This limitation is not present in STEM techniques. Atomic resolution vibrational STEM-EELS of single defects or impurities, with sensitivity to isotopic composition down to the nanoscale and nanoscale phonon dynamics, are among the breakthroughs enabled by the new technology [5–9]. Magnons, which play a crucial role in the emerging field of magnonics [10], represent another type of low-energy excitation that holds promise for measurement with this technique in the near future [11,12].

Theoretical frameworks are crucial for modeling and understanding the observed low-energy spectra, providing a foundational basis for the interpretation of experiments. However, existing computational approaches to electron scattering often rely on restrictive approximations, making quantitative comparisons with experiments challenging. These approaches are frequently confined to first-order perturbative treatments or semiclassical limits. Moreover, they frequently lack one or more important aspects of electron scattering, such as energy resolution, multiple phonon scattering, multiphonon scattering [13], dynamical diffraction, and momentum-transfer selectivity [6,14–26].

In this Letter, we show that, via the time autocorrelation of the electron beam wave function, it is possible to describe angle-resolved phonon energy loss and energy gain processes in transmission electron microscopy, including processes involving multiple phonons, the effects of temperature, and dynamical diffraction. Furthermore, we show how to extend the method to simulate angle-resolved magnon EELS and EEGS. Moreover, by its nature, this approach is computationally efficient and easy to deploy on parallel computers.

We first build the method within the framework of the quantum excitation of phonons (QEP) model [21,22]. As such, our method described below inherits all the flexibility as well as approximations assumed in the QEP model. The key step of QEP is an approximation akin to Born-Oppenheimer theory. The method then introduces the concept of configurations, denoted as $\boldsymbol{\tau}$, which are composite vectors comprising the positions of all nuclei in the system. It also involves an auxiliary electron-beam wave function, denoted as $\phi(\mathbf{r},\boldsymbol{\tau})$, or its position-to-momentum Fourier transform $\phi(\mathbf{q},\boldsymbol{\tau})$, which parametrically depends on the configuration $\boldsymbol{\tau}$. For any given arbitrary configuration $\boldsymbol{\tau}$, the auxiliary electron-beam wave function can be calculated, for example, by a standard multislice method [21,22,27].

Although the QEP model operates with fixed positions of nuclei, it provides a rigorous quantum mechanical treatment considering all possible crystal states $|\mathbf{n}\rangle$, where $\mathbf{n}$ is a composite vector describing the state of the crystal in Fock space. Thus, $\mathbf{n}$ consists of non-negative integers, expressing the number of excited quanta of all available

*Contact author: angel.castellanos.research@gmail.com
†Contact author: paul.zeiger@physics.uu.se
‡Contact author: jan.rusz@physics.uu.se

vibrational modes. The amplitude of probability for a configuration $\boldsymbol{\tau}$ to be realized in the crystal state $|\mathbf{n}\rangle$ of energy $E_{\mathbf{n}}$ is expressed through the crystal wave functions $a_{\mathbf{n}}(\boldsymbol{\tau}) = \langle \boldsymbol{\tau}|\mathbf{n}\rangle$, which can be written as a product of real-valued Hermite polynomials [22]. Within this formalism, the QEP model provides the following expression for the inelastically scattered wave corresponding to a transition of the crystal from state $|\mathbf{n}\rangle$ to state $|\mathbf{m}\rangle$:

$$\psi_{\mathbf{nm}}(\mathbf{q}) = \int a^*_{\mathbf{m}}(\boldsymbol{\tau})\phi(\mathbf{q},\boldsymbol{\tau})a_{\mathbf{n}}(\boldsymbol{\tau})d\boldsymbol{\tau}; \tag{1}$$

see, for example, Eq. (15) in Ref. [22]. By introducing the "beam transmission operator" $\hat{\phi}(\mathbf{q})$, defined by $\langle \boldsymbol{\tau}|\hat{\phi}(\mathbf{q})|\boldsymbol{\tau}'\rangle = \phi(\mathbf{q},\boldsymbol{\tau})\delta(\boldsymbol{\tau}-\boldsymbol{\tau}')$, Eq. (1) can be concisely rewritten using Dirac notation as $\psi_{\mathbf{nm}}(\mathbf{q}) = \langle \mathbf{m}|\hat{\phi}(\mathbf{q})|\mathbf{n}\rangle$.

Within this notation, the total scattering cross section is given in the QEP model as [22]

$$I_{\mathrm{tot}}(\mathbf{q}) = \frac{1}{Z}\sum_{\mathbf{n},\mathbf{m}} e^{-\beta E_{\mathbf{n}}}|\langle \mathbf{m}|\hat{\phi}(\mathbf{q})|\mathbf{n}\rangle|^2 \tag{2}$$

$$= \frac{1}{Z}\sum_{\mathbf{n}} e^{-\beta E_{\mathbf{n}}}\langle \mathbf{n}|\hat{\phi}^{\dagger}(\mathbf{q})\hat{\phi}(\mathbf{q})|\mathbf{n}\rangle$$

$$= \int d\boldsymbol{\tau}\left[\frac{1}{Z}\sum_{\mathbf{n}} e^{-\beta E_{\mathbf{n}}}|a_{\mathbf{n}}(\boldsymbol{\tau})|^2\right]|\phi(\mathbf{q},\boldsymbol{\tau})|^2, \tag{3}$$

where $Z = \sum_{\mathbf{n}} e^{-\beta E_{\mathbf{n}}}$, $\beta = (k_B T)^{-1}$, k_B is the Boltzmann constant, and the expression in square brackets represents the thermally averaged probability $P_T(\boldsymbol{\tau})$ that the system is in the configuration $\boldsymbol{\tau}$ at temperature T. The expression (3) is formally equivalent to the frozen phonon model [28], where $|\phi(\mathbf{q},\boldsymbol{\tau})|^2$ is averaged over random uncorrelated samples from the configuration space, respecting the probability distribution $P_T(\boldsymbol{\tau})$.

The given expressions for I_{tot} yield the total scattered intensity, encompassing the sum over all possible elastic and inelastic transitions. However, they do not provide spectroscopic information. Moreover, Eq. (1) expresses the inelastic wave in a manner that prevents introducing any form of probability for the configuration $\boldsymbol{\tau}$, since the product $a^*_{\mathbf{m}}(\boldsymbol{\tau})a_{\mathbf{n}}(\boldsymbol{\tau})$ is a real number that can be negative.

Nevertheless, it is possible to extract the spectroscopic information starting from Eq. (2): since the transition from state $|\mathbf{n}\rangle$ to state $|\mathbf{m}\rangle$ corresponds to an energy loss (or gain) $E = E_{\mathbf{m}} - E_{\mathbf{n}}$, the transitions can be formally sorted on the energy axis by including $\delta(E_{\mathbf{m}} - E_{\mathbf{n}} - E)$ to associate individual crystal state transitions with a specific energy transfer E. Therefore,

$$I_{\mathrm{tot}}(\mathbf{q}) = \int I(\mathbf{q},E)dE, \tag{4}$$

where

$$I(\mathbf{q},E) = \frac{1}{Z}\sum_{\mathbf{n},\mathbf{m}} e^{-\beta E_{\mathbf{n}}}|\langle \mathbf{m}|\hat{\phi}(\mathbf{q})|\mathbf{n}\rangle|^2\delta(E_{\mathbf{m}} - E_{\mathbf{n}} - E)$$

$$= \sum_{\mathbf{n},\mathbf{m}}\frac{e^{-\beta E_{\mathbf{n}}}}{Z}\int_{-\infty}^{\infty}\frac{e^{\frac{i}{\hbar}(E_{\mathbf{m}}-E_{\mathbf{n}}-E)t}}{2\pi\hbar}|\langle \mathbf{m}|\hat{\phi}(\mathbf{q})|\mathbf{n}\rangle|^2 dt$$

$$= \sum_{\mathbf{n}}\frac{e^{-\beta E_{\mathbf{n}}}}{Z}\int_{-\infty}^{\infty}\frac{e^{-\frac{i}{\hbar}Et}}{2\pi\hbar}\langle \mathbf{n}|\hat{\phi}^{\dagger}(\mathbf{q})\hat{U}_c^{\dagger}(t)\hat{\phi}(\mathbf{q})\hat{U}_c(t)|\mathbf{n}\rangle dt$$

$$= \sum_{\mathbf{n}}\frac{e^{-\beta E_{\mathbf{n}}}}{Z}\int_{-\infty}^{\infty}\frac{e^{-\frac{i}{\hbar}Et}}{2\pi\hbar}\langle \mathbf{n}|\hat{\phi}^{\dagger}(\mathbf{q},0)\hat{\phi}(\mathbf{q},t)|\mathbf{n}\rangle dt$$

$$= \int_{-\infty}^{\infty}\frac{e^{-\frac{i}{\hbar}Et}}{2\pi\hbar}\frac{1}{Z}\mathrm{Tr}\left[e^{-\beta\hat{H}_c}\hat{\phi}^{\dagger}(\mathbf{q},0)\hat{\phi}(\mathbf{q},t)\right]dt \tag{5}$$

$$= \int_{-\infty}^{\infty}\frac{e^{-\frac{i}{\hbar}Et}}{2\pi\hbar}c_{\phi\phi}(t)dt$$

$$= c_{\phi\phi}(E), \tag{6}$$

in which $\hat{U}_c(t) = e^{-(i/\hbar)\hat{H}_c t}$ is the crystal time-evolution operator, $c_{\phi\phi}(t) = (1/Z)\mathrm{Tr}[e^{-\beta\hat{H}_c}\hat{\phi}^{\dagger}(\mathbf{q},0)\hat{\phi}(\mathbf{q},t)]$ is the quantum-mechanical time autocorrelation function of the operator $\hat{\phi}(\mathbf{q})$ in Heisenberg representation, and $c_{\phi\phi}(E)$ the time-to-energy Fourier transform of $c_{\phi\phi}(t)$. Because of the central importance of the time autocorrelation of auxiliary wave (TACAW) functions, we refer to this approach as the "TACAW method".

Correlation functions that depend on the dynamics of nuclei [29] are often approximated using molecular dynamics (MD) methods or, alternatively, by ring-polymer molecular dynamics, which incorporates zero-point-energy effects of nuclei [30]. These methods yield a Kubo-transformed correlation function [31], expressed in our case as

$$\tilde{c}_{\phi\phi}(t) = \frac{1}{\beta Z}\int_0^{\beta}\mathrm{Tr}\left[e^{-(\beta-\lambda)\hat{H}_c}\hat{\phi}^{\dagger}(\mathbf{q},0)e^{-\lambda\hat{H}_c}\hat{\phi}(\mathbf{q},t)\right]d\lambda. \tag{7}$$

The following exact relation holds between the time-to-energy Fourier transforms of the two aforementioned correlation functions [30,32],

$$c_{\phi\phi}(E) = \frac{\beta E}{1-e^{-\beta E}}\tilde{c}_{\phi\phi}(E), \tag{8}$$

which allows the recovery of the initial correlation function appearing in Eq. (6).

The configurational average in the correlation function is approximated through a time average over a classical trajectory. Employing the convolution theorem, $\tilde{c}_{\phi\phi}(E)$ can then be obtained as the squared amplitude of the time-to-energy Fourier transform of the time-dependent multislice wave function $\phi_{\mathrm{MD}}(\mathbf{q},t)$, whose time dependence is realized via its parametric dependence on the

position of atoms, which naturally depends on time in a MD simulation. Therefore,

$$I(\mathbf{q},E) \propto \frac{\beta E}{1-e^{-\beta E}} |\phi_{\mathrm{MD}}(\mathbf{q},E)|^2. \tag{9}$$

While this approximation is exact for harmonic potentials and operators linear in position or momentum, errors in $\tilde{c}_{\phi\phi}(t)$ due to neglected quantum phases become more significant for larger times t beyond these conditions [30,33]. Typically, a thermal time $\beta\hbar$ serves as a benchmark beyond which the correlation functions calculated by MD methods start losing their accuracy [30].

We would like to point out that it is conceivable to calculate dynamics of nuclei and auxiliary wave functions using charge distributions derived from more sophisticated models such as Car-Parrinello [34] or *ab initio* molecular dynamics [35], or even time-dependent density functional theory-based molecular dynamics [36,37]. Nevertheless, our focus in this Letter is not on achieving a precise electronic structure description of the sample. Instead, we prioritize an accurate representation of the interaction between the high-energy beam electron and the sample.

Now, following the derivation and discussion above, we describe a procedure to simulate spectra. In the first step, a sufficiently long MD trajectory of a structure's supercell is calculated using empirical, machine learning, or even *ab initio* interatomic forces. The length of the MD trajectory t_{tot} determines the lowest nonzero vibrational energy $E_{\mathrm{min}} = 2\pi\hbar/t_{\mathrm{tot}}$ that can be obtained via the discrete Fourier transform, which matches then the frequency resolution of the calculated spectra. In contrast to frozen phonon methods [28,38], where the atomic displacements $\boldsymbol{\tau}_i$ in structure snapshots should be uncorrelated, here the snapshots are taken at short time intervals $\Delta t \sim 10^{-14}$ s to ensure that the maximum energy $E_{\mathrm{max}} = \pi\hbar/\Delta t$ in the discrete Fourier transform is greater than the highest energies in the phonon density of states. Therefore, subsequent snapshots have in general strongly correlated atomic displacements.

In the second step, the electron beam is propagated through individual snapshots, for example, using a multislice method [27,39]. Accumulating a set of exit wave functions for all snapshots results in a three-dimensional dataset $\phi_{\mathrm{MD}}(q_x,q_y,t)$, which is Fourier transformed from the time to the energy domain, producing $\phi_{\mathrm{MD}}(q_x,q_y,E)$. The squared amplitude of this object gives the approximate $\tilde{c}_{\phi\phi}(E)$, which is then converted to $c_{\phi\phi}(E)$ via Eq. (8), yielding $I(\mathbf{q},E)$ of Eq. (6) up to a normalization factor. A convenient choice is to work with a fractional intensity, where

$$\iint I(\mathbf{q},E)\,d\mathbf{q}\,dE \overset{!}{=} 1,$$

which is then imposed on the $c_{\phi\phi}(E)$ evaluated on a finite numerical grid of momentum and energy transfers. The integral over energies covers both negative (energy gains) and positive values (energy losses).

To improve the statistics, it is typically necessary to average $c_{\phi\phi}(E)$ over several MD trajectories. Various strategies can be employed for this purpose. One approach involves simulating a canonical ensemble from which several uncorrelated snapshots of the phase space (positions and momenta) are selected. These snapshots would then serve as starting points for separate microcanonical MD calculations. The advantage of this strategy is that there are no forces acting on the atoms other than those dictated by the interatomic potential. An alternative approach consists of simulating a single longer canonical MD trajectory using Langevin dynamics with low damping. Segments of this trajectory can then be used to evaluate individual $I(\mathbf{q},E)$ for subsequent averaging. Mild damping minimally affects the system dynamics, typically blurring the phonon density of states [24], while directly sampling the canonical ensemble assumed in Eq. (5).

We exhibit an implementation of the TACAW method by simulating thermal diffuse scattering for a silicon crystal, as well as electron energy loss and gain spectra arising from phonon excitations in widely studied hexagonal boron nitride (hBN). We show that it provides full momentum- and energy-resolved $I(\mathbf{q},E)$ information, including the elastic channel, as well as the energy loss and gain channels, consistent with the results of the frequency-resolved frozen phonon multislice method (FRFPMS; [23]). Furthermore, the energy integral of $c_{\phi\phi}(E)$ matches closely the results of the standard QEP method applied to snapshots of the correlated motion of atoms.

MD simulations for silicon [40] were performed on a $7\times7\times92$ supercell of cubic unit cells of silicon, with the x, y, and z directions of the cell aligned with the [100], [010], and [001] directions, respectively, and a lattice parameter of 5.4773 Å, which was obtained as an average lattice parameter in a NPT simulation at temperature $T = 300$ K and zero pressure. [41].

Similarly, MD simulations were performed on a $8\times14\times30$ supercell of the orthogonal unit cell of hBN in AA' stacking with lattice parameters $a = 1.447$ Å and $c = 6.736$ Å, which were determined in a NPT ensemble run on a $8\times14\times6$ supercell, similar to silicon. [44].

Figure 1 shows the diffraction pattern for our silicon model illuminated by a 60 kV plane-wave electron beam obtained from Eq. (4), FRFPMS, and QEP calculations. The most striking difference concerns the FRFPMS method, predicting intensities that decline with increasing scattering angle faster than in all other methods. FRFPMS has been shown to provide an accurate description of single-phonon excitations, while multiphonon processes are to a large extent missing [26]. The close numerical match between Eq. (4) and QEP methods suggests that the

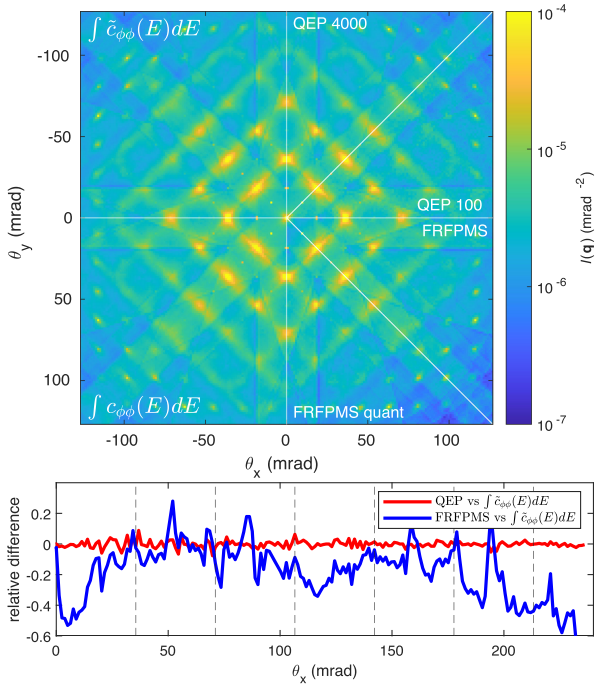

FIG. 1. Top panel: diffraction pattern of a 50 nm thick silicon crystal in [001] zone axis. Individual segments show an energy integral of $\tilde{c}_{\phi\phi}(E)$ and $c_{\phi\phi}(E)$, results of the standard QEP method using 100 evenly spaced snapshots taken every 1 ps (QEP 100) or using 4000 snapshots taken every 25 fs (QEP 4000), and finally the results of an energy integral of FRFPMS method as well as FRFPMS with quantum statistics corrections [FRFPMS quant; see Eq. (53) in Ref. [26]]. Bottom panel: relative difference (difference divided by sum) of line profiles extracted from models indicated in the legend along the $\theta_y = 0$ line. Vertical dashed lines indicate positions of Bragg spots $(2k, 0, 0)$.

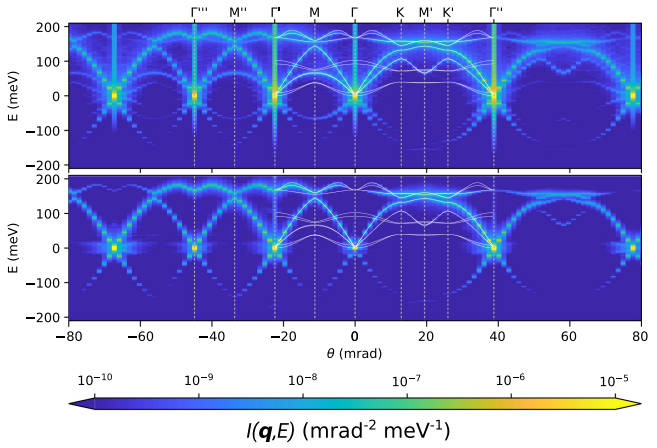

FIG. 2. Top: phonon dispersion $I(\mathbf{q}, E)$ of a 20 nm thick hBN in [0001] zone axis along the two distinct directions Γ-M-Γ′ and Γ-K-M′-K′-Γ″ (white curves) computed according to Eqs. (6)–(9). Bottom: corresponding FRFPMS calculation, including quantum corrections as proposed in Ref. [26].

intensity missing in FRFPMS is due to such multiphonon processes. The more detailed view offered by relative differences shown in the bottom panel of Fig. 1 reveals that FRFPMS underestimates also the inelastic intensity in the closest vicinity of the direct beam. We defer a more detailed discussion of the observed differences to future research.

In order to highlight the energy loss and gain information provided by the TACAW method, we show in the top panel of Fig. 2 a visualization of the scattering cross section for our hBN model structure on selected planes within the (q_x, q_y, E) space, and compare it with corresponding results of FRFPMS calculations (bottom panel). In both cases, the intensities show local maxima following the characteristic features of the phonon band dispersion of bulk hBN [48]. The match between both methods is very close for longitudinal acoustical and longitudinal optical modes, except for the higher energy resolution provided by $c_{\phi\phi}(E)$ and the appearance of background intensity, which we ascribe to processes involving excitations of multiple phonons, in analogy with the analysis of inelastic neutron scattering [51]. Notably, unlike the FRFPMS results, the top panel aligns with experimental observations [2,52], showing that the intensity of transverse phonon bands is comparable to that of longitudinal ones. Investigating this difference between FRFPMS and the TACAW method, particularly in the context of multiple scattering, is important but requires further study beyond the scope of this Letter.

Finally, we calculate EELS and EEGS due to excitations of magnons. Leveraging the formal analogies between phonons and magnons, we draw parallels as follows. Configurations $\boldsymbol{\tau}$ representing atomic displacements are reinterpreted as configurations of tilts of magnetic moments; crystal states $|\mathbf{n}\rangle$ become Fock space vectors of magnon mode occupation numbers; the auxiliary electron-beam wave function $\phi(\mathbf{q}, \boldsymbol{\tau})$ is computed using a magnetic-field-aware method, such as the Pauli multislice method [53,54]; and the MD calculations are substituted with atomistic spin dynamics calculations [55]. Furthermore, timescales and energy scales of phonon and magnon dynamics are within the same orders of magnitude. These analogies were already exploited in our previous works [11,12], and are extended here to the spectroscopic domain. As a model system for magnon simulations, we selected bcc iron. Following the methodology outlined in Ref. [12], atomistic spin dynamics simulations [56] were conducted on a $20 \times 20 \times 70$ supercell of bcc iron unit cells with a lattice parameter of 2.87 Å (i.e., with a thickness of 20 nm) and magnetic moments of 2.30 μ_B (where μ_B is the Bohr magneton), computed *ab initio* along with exchange interactions using the scalar-relativistic SPRKKR code [57,58].

Figure 3 presents a visualization of $I(\mathbf{q}, E)$. Similar to the phonon case, the energy gain part of the spectra gradually diminishes with increasing energy transfer E, in contrast to the energy loss portion. Also, the characteristic

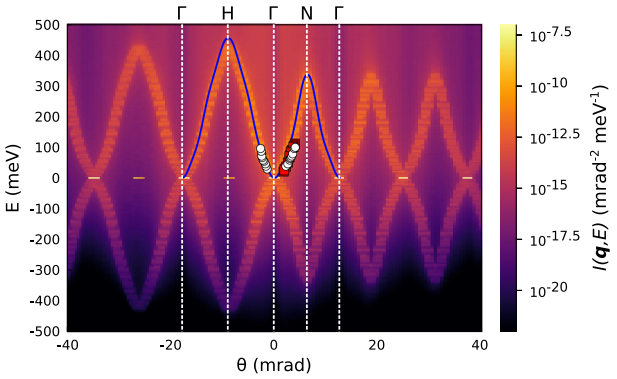

FIG. 3. $I(\mathbf{q}, E)$ for inelastic magnon scattering on 20 nm thick bcc Fe. The blue curve corresponds to the adiabatic magnon dispersion, while the scattered points are experimental neutron scattering data from Ref. [61]. The red squares come from pure Fe, while the white circles correspond to Fe with 4-at.% of Si.

features of magnon band dispersions are revealed by the local maxima of the intensities. This is highlighted by the overlap of such maxima with the magnon dispersion at 0 K [60] (blue curve) and the experimental neutron scattering data from Ref. [61].

In conclusion, we have introduced TACAW, a method for calculating angle-resolved electron energy loss spectra resulting from phonon or magnon excitations. This approach extends the quantum excitation of phonons model into the energy-loss and energy-gain domains, includes multiple inelastic events, and is straightforward to implement, adding a robust and efficient theoretical tool to the flourishing field of ultralow-energy–loss spectroscopy.

Acknowledgments—We acknowledge the support of the Swedish Research Council (Grant No. 2021-03848), Olle Engkvist's foundation (Grant No. 214-0331), STINT (Grant No. CH2019-8211), and Knut and Alice Wallenbergs' foundation (Grant No. 2022.0079). The simulations were enabled by resources provided by the National Academic Infrastructure for Supercomputing in Sweden (NAISS) at NSC Centre partially funded by the Swedish Research Council through Grant Agreement No. 2022-06725.

[1] O. L. Krivanek *et al.*, Vibrational spectroscopy in the electron microscope, Nature (London) **514**, 209 (2014).
[2] B. Plotkin-Swing *et al.*, Hybrid pixel direct detector for electron energy loss spectroscopy, Ultramicroscopy **217**, 113067 (2020).
[3] V. U. Nazarov, F. Alharbi, T. S. Fisher, and S. Kais, Time-dependent density functional theory of coupled electronic lattice motion in quasi-two-dimensional crystals, Phys. Rev. B **89**, 195423 (2014).
[4] V. U. Nazarov, V. M. Silkin, and E. E. Krasovskii, Probing mesoscopic crystals with electrons: One-step simultaneous inelastic and elastic scattering theory, Phys. Rev. B **96**, 235414 (2017).
[5] X. Yan *et al.*, Single-defect phonons imaged by electron microscopy, Nature (London) **589**, 65 (2021).
[6] F. S. Hage, G. Radtke, D. M. Kepaptsoglou, M. Lazzeri, and Q. M. Ramasse, Single-atom vibrational spectroscopy in the scanning transmission electron microscope, Science **367**, 1124 (2020).
[7] J. A. Hachtel, J. Huang, I. Popovs, S. Jansone-Popova, J. K. Keum, J. Jakowski, T. C. Lovejoy, N. Dellby, O. L. Krivanek, and J. C. Idrobo, Identification of site-specific isotopic labels by vibrational spectroscopy in the electron microscope, Science **363**, 525 (2019).
[8] R. Senga, Y.-C. Lin, S. Morishita, R. Kato, T. Yamada, M. Hasegawa, and K. Suenaga, Imaging of isotope diffusion using atomic-scale vibrational spectroscopy, Nature (London) **603**, 68 (2022).
[9] C. A. Gadre *et al.*, Nanoscale imaging of phonon dynamics by electron microscopy, Nature (London) **606**, 292 (2022).
[10] A. Barman *et al.*, The 2021 magnonics roadmap, J. Phys. Condens. Matter **33**, 413001 (2021).
[11] K. Lyon, A. Bergman, P. Zeiger, D. Kepaptsoglou, Q. M. Ramasse, J. C. Idrobo, and J. Rusz, Theory of magnon diffuse scattering in scanning transmission electron microscopy, Phys. Rev. B **104**, 214418 (2021).
[12] J. Á. Castellanos-Reyes, P. Zeiger, A. Bergman, D. Kepaptsoglou, Q. M. Ramasse, J. C. Idrobo, and J. Rusz, Unveiling the impact of temperature on magnon diffuse scattering detection in the transmission electron microscope, Phys. Rev. B **108**, 134435 (2023).
[13] With "multiphonon scattering," we refer to the situation in which the electron (from the electron beam) scatters creating several phonons in a single inelastic event. "Multiple phonon scattering" corresponds to multiple inelastic scattering events, in which the electron creates one or more phonons each time.
[14] R. J. Nicholls, F. S. Hage, D. G. McCulloch, Q. M. Ramasse, K. Refson, and J. R. Yates, Theory of momentum-resolved phonon spectroscopy in the electron microscope, Phys. Rev. B **99**, 094105 (2019).
[15] R. Senga, K. Suenaga, P. Barone, S. Morishita, F. Mauri, and T. Pichler, Position and momentum mapping of vibrations in graphene nanostructures, Nature (London) **573**, 247 (2019).
[16] L. J. Allen and T. W. Josefsson, Inelastic scattering of fast electrons by crystals, Phys. Rev. B **52**, 3184 (1995).
[17] A. V. Martin, S. D. Findlay, and L. J. Allen, Model of phonon excitation by fast electrons in a crystal with correlated atomic motion, Phys. Rev. B **80**, 024308 (2009).
[18] B. D. Forbes and L. J. Allen, Modeling energy-loss spectra due to phonon excitation, Phys. Rev. B **94**, 014110 (2016).
[19] C. Dwyer, Prospects of spatial resolution in vibrational electron energy loss spectroscopy: Implications of dipolar scattering, Phys. Rev. B **96**, 224102 (2017).
[20] P. Rez and A. Singh, Lattice resolution of vibrational modes in the electron microscope, Ultramicroscopy **220**, 113162 (2021).
[21] B. D. Forbes, A. V. Martin, S. D. Findlay, A. J. D'Alfonso, and L. J. Allen, Quantum mechanical model for phonon excitation in electron diffraction and imaging using a Born-Oppenheimer approximation, Phys. Rev. B **82**, 104103 (2010).

[22] N. R. Lugg, B. D. Forbes, S. D. Findlay, and L. J. Allen, Atomic resolution imaging using electron energy-loss phonon spectroscopy, Phys. Rev. B **91**, 144108 (2015).
[23] P. M. Zeiger and J. Rusz, Efficient and versatile model for vibrational STEM-EELS, Phys. Rev. Lett. **124**, 025501 (2020).
[24] P. M. Zeiger and J. Rusz, Frequency-resolved frozen phonon multislice method and its application to vibrational electron energy loss spectroscopy using parallel illumination, Phys. Rev. B **104**, 104301 (2021).
[25] H. Lourenço-Martins, A. Lubk, and M. Kociak, Bridging nano-optics and condensed matter formalisms in a unified description of inelastic scattering of relativistic electron beams, SciPost Phys. **10**, 031 (2021).
[26] P. M. Zeiger, J. Barthel, L. J. Allen, and J. Rusz, Lessons from the harmonic oscillator: Reconciliation of the frequency-resolved frozen phonon multislice method with other theoretical approaches, Phys. Rev. B **108**, 094309 (2023).
[27] J. M. Cowley and A. F. Moodie, The scattering of electrons by atoms and crystals. I. A new theoretical approach, Acta Crystallogr. **10**, 609 (1957).
[28] R. F. Loane, P. Xu, and J. Silcox, Thermal vibrations in convergent-beam electron diffraction, Acta Crystallogr. Sect. A **47**, 267 (1991).
[29] L. Van Hove, Correlations in space and time and Born approximation scattering in systems of interacting particles, Phys. Rev. **95**, 249 (1954).
[30] I. R. Craig and D. E. Manolopoulos, Quantum statistics and classical mechanics: Real time correlation functions from ring polymer molecular dynamics, J. Chem. Phys. **121**, 3368 (2004).
[31] R. Kubo, Statistical-mechanical theory of irreversible processes. I. General theory and simple applications to magnetic and conduction problems, J. Phys. Soc. Jpn. **12**, 570 (1957).
[32] P. H. Berens and K. R. Wilson, Molecular dynamics and spectra. I. Diatomic rotation and vibration, J. Chem. Phys. **74**, 4872 (1981).
[33] W. H. Miller, The semiclassical initial value representation: A potentially practical way for adding quantum effects to classical molecular dynamics simulations, J. Phys. Chem. A **105**, 2942 (2001).
[34] R. Car and M. Parrinello, Unified approach for molecular dynamics and density-functional theory, Phys. Rev. Lett. **55**, 2471 (1985).
[35] T. D. Kühne, M. Krack, F. R. Mohamed, and M. Parrinello, Efficient and accurate Car-Parrinello-like approach to Born-Oppenheimer molecular dynamics, Phys. Rev. Lett. **98**, 066401 (2007).
[36] M. D. Hack and D. G. Truhlar, Nonadiabatic trajectories at an exhibition, J. Phys. Chem. A **104**, 7917 (2000).
[37] X.-P. Wang, X.-B. Li, N.-K. Chen, J. Bang, R. Nelson, C. Ertural, R. Dronskowski, H.-B. Sun, and S. Zhang, Time-dependent density-functional theory molecular-dynamics study on amorphization of Sc-Sb-Te alloy under optical excitation, npj Comput. Mater. **6**, 31 (2020).
[38] D. A. Muller, B. Edwards, E. J. Kirkland, and J. Silcox, Simulation of thermal diffuse scattering including a detailed phonon dispersion curve, Ultramicroscopy **86**, 371 (2001).
[39] J. Barthel, Dr. Probe: A software for high-resolution STEM image simulation, Ultramicroscopy **193**, 1 (2018).
[40] A. P. Thompson *et al.*, LAMMPS—A flexible simulation tool for particle-based materials modeling at the atomic, meso, and continuum scales, Comput. Phys. Commun. **271**, 108171 (2022).
[41] The machine learning SNAP interatomic potential [42] for silicon from Ref. [43] was employed. A time step of 0.5 fs was chosen, and after 5000 steps of thermalization, a 0.1 ns trajectory at 300 K was generated to capture snapshots. A relatively low Langevin damping of 0.5 ps was used to minimize its impact on the dynamics. In total, 4000 snapshots were generated with a $\Delta t = 25$ fs, allowing one to reach vibrational frequencies of up to 20 THz (~83 meV). For all of them, we have calculated the exit wave functions using DrProbe [39] on a numerical grid of 560×560 using 736 slices across the whole thickness of the supercell. To evaluate $I(\mathbf{q}, E)$, we have averaged over 79 sets of 100 consecutive snapshots (i.e., $T = 2.5$ ps), mutually offset by 50 snapshots. In this way, all the 4000 snapshots were utilized twice, except for the first and the last 50 snapshots. The same MD trajectory was used for FRFPMS calculations, performed on a grid of 1 THz wide frequency bins covering the range of up to 18 THz. Within each frequency bin, 128 snapshots have been generated by band-pass filtering the MD trajectory.
[42] A. Thompson, L. Swiler, C. Trott, S. Foiles, and G. Tucker, Spectral neighbor analysis method for automated generation of quantum-accurate interatomic potentials, J. Comput. Phys. **285**, 316 (2015).
[43] Y. Zuo, C. Chen, X. Li, Z. Deng, Y. Chen, J. Behler, G. Csányi, A. V. Shapeev, A. P. Thompson, M. A. Wood, and S. P. Ong, Performance and cost assessment of machine learning interatomic potentials, J. Phys. Chem. A **124**, 731 (2020).
[44] The x, y, and z dimensions were aligned with the $[2\bar{1}\,\bar{1}\,0]$, $[01\bar{1}0]$, and [0001] directions, respectively. The interatomic potential was a machine-learned, so-called Gaussian approximation potential for hBN [45–47] and the time step was set to 0.5 fs in all simulations. For the results shown here, one trajectory of 100 ps was simulated after an initial thermalization of 10 ps employing a Langevin thermostat with a damping of 0.5 ps. The positions of all atoms were saved every 7.5 fs, which allows reaching vibrational frequencies up to 66.67 THz (~276 meV) for a total of 13 332 snapshots. As in the case of silicon, we calculated the beam exit wave function for all snapshots using DrProbe on a numerical grid of 560×560, albeit using only 500 slices across the whole thickness of the supercell. $I(\mathbf{q}, E)$ was evaluated as an average over 79 sets of 332 consecutive snapshots (i.e., $T = 2.49$ ps), mutually offset by 116 snapshots. Snapshots for FRFPMS simulations were sampled using band-pass filtering for 51 energy bins between 0 and 50 THz with a width of 1 THz per bin. The 0 THz bin considers thereby only frequencies between 0.0 to 0.5 THz.
[45] A. P. Bartók, M. C. Payne, R. Kondor, and G. Csányi, Gaussian approximation potentials: The accuracy of quantum mechanics, without the electrons, Phys. Rev. Lett. **104**, 136403 (2010).

[46] A. P. Bartók, R. Kondor, and G. Csányi, On representing chemical environments, Phys. Rev. B **87**, 184115 (2013).
[47] F. L. Thiemann, P. Rowe, E. A. Müller, and A. Michaelides, Machine learning potential for hexagonal boron nitride applied to thermally and mechanically induced rippling, J. Phys. Chem. C **124**, 22278 (2020).
[48] We have computed the phonon dispersion for the Gaussian approximation potential using PHONOPY with its LAMMPS interface [49,50].
[49] A. Togo, L. Chaput, T. Tadano, and I. Tanaka, Implementation strategies in PHONOPY and PHONO3PY, J. Phys. **35**, 353001 (2023).
[50] A. Togo, First-principles phonon calculations with PHONOPY and PHONO3PY, J. Phys. Soc. Jpn. **92**, 012001 (2023).
[51] J. Dawidowski, F. J. Bermejo, and J. R. Granada, Efficient procedure for the evaluation of multiple scattering and multiphonon corrections in inelastic neutron-scattering experiments, Phys. Rev. B **58**, 706 (1998).
[52] A. O'Hara, B. Plotkin-Swing, N. Dellby, J. C. Idrobo, O. L. Krivanek, T. C. Lovejoy, and S. T. Pantelides, High-temperature phonons in h-BN: Momentum-resolved vibrational spectroscopy and theory, arXiv:2310.13813.
[53] A. Edström, A. Lubk, and J. Rusz, Elastic scattering of electron vortex beams in magnetic matter, Phys. Rev. Lett. **116**, 127203 (2016).
[54] A. Edström, A. Lubk, and J. Rusz, Magnetic effects in the paraxial regime of elastic electron scattering, Phys. Rev. B **94**, 174414 (2016).
[55] O. Eriksson, A. Bergman, L. Bergqvist, and J. Hellsvik, *Atomistic Spin Dynamics: Foundations and Applications* (Oxford University Press, New york, 2017).
[56] The Uppsala atomistic spin dynamics code, UppASD, https://github.com/UppASD/UppASD (2023) last accessed 2023-11-13.
[57] H. Ebert, D. Ködderitzsch, and J. Minár, Calculating condensed matter properties using the KKR-Green's function method–recent developments and applications, Rep. Prog. Phys. **74**, 096501 (2011).
[58] Employing a time step of 0.1 fs and a Gilbert damping parameter $\alpha = 10^{-4}$, a thermalization phase of 100 000 steps was followed by a 0.02 ns trajectory at 300 K for generating snapshots. In total, 5000 snapshots were generated with a $\Delta t = 4$ fs, enabling exploration of magnon frequencies up to 125 THz (∼517 meV). The exit wave functions were computed using the Pauli multislice method on a numerical grid of 1000×1000 with 2100 slices across the supercell's thickness. A 200-kV electron probe with a 1 mrad convergence semiangle, propagating along the [001] direction, was employed. We have used the parametrized magnetic vector potential developed in Ref. [59]. The Debye-Waller factor and an absorptive optical potential (see Appendix B of Ref. [12]) were included to simulate, in first approximation, the effect of phonon excitations on elastic scattering. For the analysis of $I(\mathbf{q}, E)$, we averaged over 48 sets of 250 consecutive snapshots (i.e., $T = 1.0$ ps), mutually offset by 100 snapshots.
[59] K. Lyon and J. Rusz, Parameterization of magnetic vector potentials and fields for efficient multislice calculations of elastic electron scattering, Acta Crystallogr. Sect. A **77**, 509 (2021).
[60] Derived from the adiabatic magnon spectrum [55] (in the $\Gamma \to H \to \Gamma$ path for the horizontal direction, $\theta_y = 0$, and in the $\Gamma \to N \to \Gamma$ for the $\theta_y = -\theta_x$ diagonal direction).
[61] H. A. Mook and R. M. Nicklow, Neutron scattering investigation of the magnetic excitations in iron, Phys. Rev. B **7**, 336 (1973).